BNL-216062-2020-JAAM

The effects of vanadium substitution on one-dimensional tunnel structures of cryptomelane: Combined TEM and DFT study

S. Yang, A. C. Marschilok

To be published in "NANO ENERGY"

May 2020

Interdisciplinary Science Department

Brookhaven National Laboratory

U.S. Department of Energy

USDOE Office of Science (SC), Basic Energy Sciences (BES) (SC-22)

Notice: This manuscript has been authored by employees of Brookhaven Science Associates, LLC under Contract No. DE-SC0012704 with the U.S. Department of Energy. The publisher by accepting the manuscript for publication acknowledges that the United States Government retains a non-exclusive, paid-up, irrevocable, world-wide license to publish or reproduce the published form of this manuscript, or allow others to do so, for United States Government purposes.

DISCLAIMER

This report was prepared as an account of work sponsored by an agency of the United States Government. Neither the United States Government nor any agency thereof, nor any of their employees, nor any of their contractors, subcontractors, or their employees, makes any warranty, express or implied, or assumes any legal liability or responsibility for the accuracy, completeness, or any third party's use or the results of such use of any information, apparatus, product, or process disclosed, or represents that its use would not infringe privately owned rights. Reference herein to any specific commercial product, process, or service by trade name, trademark, manufacturer, or otherwise, does not necessarily constitute or imply its endorsement, recommendation, or favoring by the United States Government or any agency thereof or its contractors or subcontractors. The views and opinions of authors expressed herein do not necessarily state or reflect those of the United States Government or any agency thereof.

The effects of vanadium substitution on one-dimensional tunnel structures of cryptomelane: Combined TEM and DFT study

Shi-Ze Yang,[1,2,†] Killian R. Tallman,[3,†] Ping Liu,[4*] Diana M. Lutz,[3] Bingjie Zhang,[3] Sung Joo Kim,[1,2] Lijun Wu,[1] Amy C. Marschilok,[2,3,5] Esther S. Takeuchi, [2,3,5] Kenneth J. Takeuchi,[3,5*] Yimei Zhu[1,6*]

[1]Condensed Matter Physics and Materials Science Department, Brookhaven National Laboratory, Upton, New York 11973, United States

[2]Energy and Photon Sciences Directorate, Brookhaven National Laboratory, Upton, New York 11973, United States

[3]Department of Chemistry, Stony Brook University, Stony Brook, New York 11794, United States

[4]Chemistry Division, Brookhaven National Laboratory, Upton, New York 11973, United States

[5]Department of Materials Science and Chemical Engineering, Stony Brook University, Stony Brook, New York 11794, United States

[6]Department of Physics and Astronomy, Stony Brook University, Stony Brook, New York 11794, United States

[†]Equal contributions by S.Z.Y. and K.R.T.

Corresponding authors: Ping Liu (pingliu3@bnl.gov), Kenneth J. Takeuchi (kenneth.takeuchi.1@stonybrook.edu) and Yimei Zhu (zhu@bnl.gov)

Abstract

Rational design of energy storage materials requires mechanistic understanding which relies on atomic scale characterization of structure and defects. Here we utilize vanadium (V)-substituted one-dimensional cryptomelane as a model material to study structural features critical to electrochemical reversibility of the cathode in lithium-ion batteries. We found the substitution of manganese (Mn) atoms in the tunnel wall with V enhances structural uniformity in the parent KMn_8O_{16} material by inhibiting formation of irregular (2×3 and 2×1) manganese oxide tunnel structures. Upon lithiation, both transmission electron microscopy (TEM) and density functional theory (DFT) reveal significant structural evolution, eventually resulting in phase separation and formation of highly reduced manganese oxide. During this process, Mn^{4+} accepts electrons donated by intercalated Li, while the V^{4+} substituent is not electrochemically reduced but acts to stabilize the tunnel framework structure. As a result, the V substituted material shows higher operating voltage and improved electrochemical reversibility. Our results highlight the benefits of V-substitution in cryptomelane, and the significance

of integrating characterization with simulation for understanding and developing design principles for lithium ion battery materials.

Key words:

Scanning transmission electron microscopy (STEM), in-situ TEM, battery, alpha-MnO_2, DFT

Main text

Lithium-ion batteries play a critical role as portable energy storage systems in modern society.[1-3] The major components of lithium-ion batteries are the cathode, anode, separator, electrolyte and binder.[2] The central scientific problem of these systems that needs to be addressed is how to scientifically advance the different components to improve the rate capability, reduce cost, increase cycle life and achieve safe operation. Since the first discovery of lithium cobalt oxide as an intercalation cathode, many other promising materials have been identified, including spinel oxides, layered oxides, olivine iron phosphate and manganese oxides.[1] Among the candidates, manganese oxides have the special advantage of low-cost. Further, the rich structural polymorphs of manganese oxide provide vast opportunities for exploring the effect of material structure on electrochemistry.[3-10] Tunnel-type (or hollandite) manganese oxide with one-dimensional Li diffusion channels is a very interesting material for studying the fundamental electrochemistry of manganese oxides.[3,5,6,11-15] Hollandite structures have attracted special attention due to the homogenous tunnel structure and moderate space within the tunnel. Different ions, such as Na^+, K^+, Ca^{2+}, Ba^{2+}, H_3O^+ or NH_4^+ , can be inserted into the tunnel to provide compensating positive charge to increase structural stability.[3]

Structural features including particle size, surface defects and volume (bulk) defects can impact the electrochemistry of battery materials.[13,16,17] Nanomaterials are beneficial for lithium-ion batteries as they provide a short Li diffusion path length.[17,18] Both surface structure and the stability of electrode materials are critical to the electrochemistry, as the surface is the interface with the electrolyte and structural stability facilitates the diffusion of Li ions from electrode to electrolyte.[19] Surface coating and doping have been generally adopted to stabilize the surface structure for high voltage battery electrode materials.[20,21] In addition, surface defects are beneficial for Li diffusion across tunnels.[13] Finally, volume (bulk) defects can be important, as demonstrated by the improved cycling performance in Ni-rich layered cathodes caused by tailoring grain boundaries within the material.[22]

In the current study, we substitute Mn atoms with V to tune the electrochemistry of cryptomelane (K_xMnO_2) from the perspective of its atomic structure. In the pristine nanorod, irregular 2×1 and 2×3 boundary tunnels are identified along with the dominant 2×2 tunnel framework. Upon V substitution, these irregular tunnel sizes are no longer observed while tunnel lengths are reduced. Electron energy loss spectroscopy (EELS) mapping shows that V dopants occupy the tunnel wall positions, directly substituting Mn atoms. In-situ and ex-situ EELS measurements show that valence change of Mn is much larger than that of V upon reduction by lithium metal. Consistent with the experimental observations, DFT simulations also reveal the substituted V ions to be in a slightly oxidized state and that upon lithiation V is reduced only slightly as compared to Mn.

Results and discussions

Here we report four samples in our study: pristine cryptomelane ($K_{0.99}Mn_8O_{16}$), 3%V-substituted cryptomelane ($K_{1.00}Mn_{7.78}V_{0.22}O_{16}$), 5%V-substituted cryptomelane ($K_{1.02}Mn_{7.63}V_{0.37}O_{16}$), and 10%V-substituted cryptomelane ($K_{0.97}Mn_{7.2}V_{0.8}O_{16}$). The chemical formulas are based on quantitative ICP-OES measurements. **Figure 1a** shows the transmission electron microscopy (TEM) images at a field view of 920 nm and STEM images along the c-axis with a field view of 7 nm. V substitution changes the nanorod length from ~1 μm in the pristine sample to less than 200 nm for the 5%V-doped sample, and the morphology changes to particle-like for the 10%V-doped sample. TEM images of each sample at a field view of 200 nm are shown in **Figure S1**. The diameters of these samples mostly range from 10 nm to 30 nm. Particle like samples start to appear at 5%V-substitution while the rod shape disappears in the 10%V-substituted samples.

The typical 2×2 tunnels of pristine cryptomelane along the c-axis is shown in **Figure 1b**. The bright spot features correspond to the Mn atomic columns (red dash circles) which form a square pattern (2×2 tunnel) and the less bright features in the center of the squares are K^+ atomic columns (purple dash circles). The contrast in scanning transmission electron microscopy (STEM) angular dark field (ADF) images is proportional to the average Z number in the column and has been widely adopted to directly identify the dopants in monolayers[23,24] and single atom catalysts.[25] Mn and V have similar atomic numbers of 25 and 23, respectively, and thus it is difficult to distinguish Mn and V atoms by ADF contrast. The 2x2 tunnel structures of the 0%V-substituted and 5%V-substituted samples were compared (**Figure S2**). Both samples show homogenous contrast at Mn positions and fluctuation of intensity at K positions. This result indicates that some tunnels might be less occupied by

K. The nanobeam electron diffraction (NBED) along the c-axis of the pure cryptomelane is shown in the inset of **Figure 1b**, with the {110} planes indexed. Some of the diffraction spots are found to split slightly, which indicates the existence of grains with close orientation. The lattice parameters from both diffraction and DFT simulations for the 0%V-substituted and 10%V-substituted samples are shown in **Table S1**. The values are in good agreement which indicates the simulation method adopted is appropriate. Irregular tunnels or grain boundaries (2×1 and 2×3 tunnels) are identified in the 0%V-substituted sample (**Figure 1c**) while only 2×2 tunnels are observed in the 3, 5, and 10%V-substituted samples (**Figure 1d**). Multiple cross-section images of the 0%V and 5%V-substituted samples were collected to obtain statistical insight (**Figure S3, S4**). On six randomly selected nanorods, the 0%V-substituted sample always has irregular tunnels (**Figure S3**) compared with no such tunnels for 5%V-substituted sample (**Figure S4**). The irregular 2×3 tunnels can be viewed as boundaries between nanorods, possibly grown from different nuclei, as indicated by the hollow void (**Figure S3**). These irregular tunnels with faster Li diffusion rates[26] are likely to be lithiated or sodiated to a deeper level, which then leads to cracks in the structure. The above results suggest that the 2×2 tunnel framework is stabilized by V substitution. As will be seen in the following, such enhancement is associated with the atomic position and electronic structure of the vanadium substituted material according to the DFT calculations.

STEM EELS results for the V, O, and Mn edges are shown in **Figure 1e-1g**. Former reports suggest that it is possible to quantify the valence of V by measuring the peak position of L_3 edge.[27] The V-L_3 peaks were fitted with a Gaussian function and compared with reference VO_2 and V_2O_5 samples. Using the linear interpolation method, the V was determined to be close to 4.6^+ for all substituted samples. The slight increase in the peak intensity around 640 eV at Mn-L edge indicates the reduction of Mn valence upon V substitution (**Figure 1g**). The L_3/L_2 intensity ratios and Mn valence are measured to be $2.04/3.6^+$ (0%V), $2.15/3.4^+$ (3%V), $2.08/3.5^+$ (5%V) and $2.08/3.5^+$ (10%V). Energy dispersive X-ray spectroscopy (EDX) mapping shows that the V dopant is distributed evenly across the nanorods and/or nanoparticles within the measurement sensitivity and accuracy (**Figure S5-S7**).

It is critical to understand the atomic position of the V dopant in the structure. Previous papers remain controversial as to whether the dopants are replacing Mn in the wall or are occupying the tunnel.[28,29] Because of the low concentration, the V-L edge EELS signal is rather weak. Electron beam damage also limits the total electron dose for each measurement. We chose the 5%V-substituted sample for high resolution mapping as the 10%V-substituted sample decomposed too quickly under the

electron beam (**Figure 2a**). The original mapping results are processed by principal component analysis to improve signal-to-noise ratio with four independent components. The elemental maps for Mn, V and K are shown in red, green and blue, respectively, with a composite of Mn-V-K, ADF image and structural models shown to the right. The raw data was summed horizontally along the tunnel direction (**Figure S8**). Higher K peak intensity appears in tunnel positions while the V peak follows the pattern of the Mn peak. Clearly, the observation suggests that V occupies the tunnel wall position, substituting the Mn atoms.

Different structural models were constructed and optimized using DFT, including pristine cryptomelane (**Figure 2b**), V-substituted cryptomelane with one Mn in the (2×2) tunnel wall replaced by V (**Figure 2c**) and V-centered cryptomelane with V located in the center of the empty (2×2) tunnel (**Figure 2d**). The relaxed lattice parameters for these three structures are shown in **Table S2**. According to the DFT-calculated formation energy (see theoretical method) for KMn_7VO_{16}, the V-centered system is more thermodynamically favorable than the V-doped system by -1.93 eV/supercell. However, such preference is decreased to -0.82 eV/supercell by stabilizing the Mn ion from Mn^{2+} (aq) to $MnSO_4$ (aq). Thus, in terms of energetics the relative stability of the KMn_7VO_{16} species strongly depends on the state of the Mn ions during synthesis. Accordingly, the selection of a precursor for Mn ions that is more stable than $MnSO_4$ (aq), e.g. $MnSO_4{\cdot}H_2O$ as reported previously[30,31], can eventually inverse the trend and tune the thermodynamic preference toward the V substitution for Mn in the tunnel wall. The presence of V (KMn_7VO_{16}, **Figure 2d**) leads to the further reduction and increased amount of Mn^{3+} as compared to KMn_8O_{16} (**Figure 2b**) based on the calculated partial density of states (PDOS**)** of Mn ions in KMn_7VO_{16} (**Figures S9**) and in the MnO_x series (**Figure S10**). As a result, the host 2×2 tunnel is destabilized, which is demonstrated by the breakage of two MnO_6 octahedra along the wall and a highly disturbed electronic structure (**Figure S9**). This is consistent with our previous study of MnO_2, showing that the highly distorted octahedra of reduced Mn is the key precursor for tunnel breaking.[32] For KMn_7VO_{16} (**Figure 2c**), the substituted V is not reduced, remaining at 4^+, according to the calculated PDOS for V ions (**Figures S10 and S11**) and the amount of reduced Mn ions remains the same as in KMn_8O_{16}. Thus, only small variation in local structure is observed. Given that, DFT predicts that if the Mn ions substituted by V can be well stabilized, the Mn position is likely preferred over the tunnel center for the V substituent, consistent with the EELS mapping observations.

Electrochemical measurements were carried out to determine the effects of vanadium substitution. Galvanostatic cycling was performed where the depth of discharge was controlled to reach an average oxidation state of $Mn^{3.25+}$ for each material, assuming all V was V^{5+}, consistent with the EELS measurement. The voltage profiles for the first and second cycle are shown in **Figure S12**. The pristine material was more polarized in both cycles, and it reached the lower voltage limit of 0.5V prior to reaching the target Mn oxidation state in the second cycle. The V-substituted samples maintained higher voltages throughout the discharge with decreased polarization. Thus, increased delivered capacity and decreased polarization are observed with increasing levels of V substitution.

In-situ lithiation experiments were carried out to further reveal the effect of V substitution on the electrochemical properties of the samples. Two samples were selected: 0%V-substituted and 5%V-substituted cryptomelane. In-situ results for the 5%V-substituted cryptomelane are shown in **Figure 3**. The in-situ experiment setup is shown in the schematic in **Figure 3a**. **Figure 3b-3f** shows the in-situ recorded TEM images at different stages of lithiation. The early stage of the lithiation, from t = 0 to 9.5 s, involves a mixture of intercalation and conversion reactions similar to what was shown in a former report.[33] The reaction front gradually advances through the nanorod and an intermediate bell-like feature can be seen at t = 5s, which causes a nanorod expansion of 9%, as shown in **Figure 3d**. The expansion in the bell-like feature is attributed to the Li concentration gradient, with more intercalation occurring at the narrow end and more conversion occurring at the wider base.[33] By the end of the early stage, the bell-like feature vanished and the nanorod had expanded by 16% normal to the tunnel. Further lithiation resulted in a kink formation. The overall morphology expansion is shown in **Figure 3g**.

The NBED pattern of the nanorod was measured before lithiation (**Figure 3h**) and at the end of the experiment (**Figure 3i**). The d-spacing of the (002) plane is measured to be 1.43 Å before lithiation and 1.51 Å after lithiation. After lithiation, an MnO-like phase formed as indicated by the appearance of MnO {220} and {111} planes (**Figure 3i**). The (002) plane of cryptomelane coincides with the MnO (220) plane indicating the preferential alignment between the two phase structures.[33] Lattice spacing of $(4\bar{2}0)$ are measured to be 2.19 Å before lithiation and 2.52 Å after lithiation. Thus, electron diffraction indicates lattice expansion of 6% along the tunnel and 15% normal to the tunnel which agrees very well with the 16% expansion measured from both TEM images (**Figure 3e**) and STEM images (**Figure S13**). STEM EELS were collected on the same nanorod before and after lithiation for V-L edge, O-K edge and Mn-L edge as shown in **Figure 3j and 3k**. The apparent peak shift of Mn-L

edge indicates the reduction of Mn valence after lithiation as compared with the standard reference samples. The Mn L_3/L_2 intensity ratios were measured based on the Pearson method as described in reference[34] and Mn valance was calculated based on the L_3/L_2 intensity ratio and calibrated with standard reference samples of MnO_2 and Mn_2O_3 (**Figure S13**). The Mn valence was calculated to be 3.5^+ before lithiation and 2.0^+ after lithiation. The V valence calculated from the V-L_3 edge peak positions changed from 4.7^+ before lithiation to 4.5^+ after lithiation. The O-K peak around 530 eV (peak1) is attributed to the transition from 1s core states to O 2p states hybridized with Mn 3d orbitals. The peak around 540 eV (peak2) is related to the hybridized O p state and Mn 4sp band above the Fermi level.[35] The relative intensity of peak1 and peak2 after lithiation resemble that of Mn_2O_3, yet the peak2 energy is closer to MnO, which indicates that the oxygen coordination environment changed drastically after lithiation and agrees with the reduction in Mn valence. More in-situ recorded lithiation images are provided in **Figure S14** and **S15** which show similar reaction front dynamics.

DFT simulations were performed to model the lithiation process of KMn_7VO_{16} with 0 to 6 Li atoms per supercell, $Li_{x\ (x=0\text{-}6)}KMn_7VO_{16}$ (**Figure 2c, Figure 4a-4f**). The lattice parameters are shown in **Table S2**. A volume expansion of 18.9% is observed in the structure with 6 inserted Li atoms which agrees well with the experimentally observed expansion of 16% normal to the tunnel. With increasing lithiation of the structure, the tunnels are gradually detached, and the valence of Mn is continuously reduced. At x=1, Li prefers to be intercalated into the 5-coordinated 8h site and 4-coordinated 8h' site of the empty 2×2 tunnel for KMn_8O_{16} and KMn_7VO_{16}, respectively, which is accompanied by the reduction of an additional Mn^{4+} to Mn^{3+} (**Figures S10 and S11**) while maintaining the tunnel structure. Upon the insertion of a second Li to the same 2×2 tunnel as the first Li (to an opposite 8h'/8h site yielding the same lithiation locations at Li_2, shown in **Figure 4e**) for both cases, the Mn^{4+} to Mn^{3+} reduction continues and the Li-intercalated 2×2 tunnel breaks via two pairs of corner-sharing octahedra which strongly interact with Li. In this way, K-centered 2×2 tunnel rows stacked in a layer are formed, where Li ions fill the space between the layers. Starting at x = 3, KMn_8O_{16} and KMn_7VO_{16} behave differently. For KMn_8O_{16}, Li continues to occupy the interlayer positions until it is fully filled at x =5 (**Figure S16**), and the sixth lithium is inserted in to the 8h site of a 2×2 tunnel centered by K. In case of KMn_7VO_{16}, the stability of the K-centered 2×2 tunnel is increased, as it is now able to accommodate Li^+ ions up to x = 5 while maintaining an intact tunnel structure. During the lithiation process, the substituted V is only slightly reduced (**Figures S10 and S11**) and shows a strong interaction with the neighboring unreduced MnO_6 octahedra via an edge-sharing conformation (**Figure 4f**). Finally,

although the DFT calculations cannot simulate the phase separation to MnO at the end stage of the lithiation, all of the Mn are 3+ at the high lithiation state of $Li_6KMn_7VO_{16}$ (**Figures S10 and S11**), where the corresponding structure is greatly distorted and does not resemble 2×2 hollandite (**Figure 4f**). Further lithiation is very likely to enable additional reduction of Mn^{3+} and form heavily reduced oxide phases, such as MnO (**Figure S10**).

The correlation between V and Mn valence from the above simulations is shown in **Figure 4g**. EELS measurements were carried out on the lithiated samples to provide further experimental understanding of the lithiation mechanism (**Figure 4h**). Both DFT and EELS results show that the valence change of V is smaller than Mn as indicated by the smaller height than width of the rectangles covering the data points. The preferential reduction of Mn over substituted V during lithiation is associated with the redistribution of electron densities introduced by V substitution. The calculated PDOS (**Figure S11**) of KMn_7VO_{16} show that the lowest unoccupied states are dominantly contributed by Mn^{4+}, which readily accepts electrons donated by lithium intercalation, while the contribution from the substituted V^{4+} is rather small. That is, Mn^{4+} is more reducible than V^{4+}, or in other words, the substituted V^{4+} is more stable than Mn^{4+} in the wall. As a result, the replacement of Mn^{4+} on the wall by a more stable V^{4+} is likely to enhance the stability of the stoichiometric tunnel structure, which explains the improved tunnel homogeneity (**Figure 1**) and observed V/Mn valence change (**Figure 4**).

DFT calculations clearly show the favorable role of V substitution in stabilizing the tunnel structure of KMn_8O_{16}. The substitution of Mn for V enables the formation of V^{4+} ions which are less reducible and more stable than the other Mn^{4+} in the tunnel wall. As a result, the formation of stoichiometric 2×2 tunnel motif is more favorable for the pristine KMn_7VO_{16} than the KMn_8O_{16}. Under lithiation conditions, Mn^{4+} acts as an electron acceptor for electrons donated by Li, while due to the unique electronic structures, the substituted V^{4+} is the structural stabilizer. The V^{4+} ions can survive and promote the stability of the tunnel structure in KMn_7VO_{16} via strong interaction with the neighboring Mn^{4+}. KMn_7VO_{16} can accommodate two Li^+ and one K^+ into the tunnel without wall breakage, while only one Li^+ ion and one K^+ ion can be hosted in the 2×2 tunnel of KMn_8O_{16}. By comparison, with doped V positioned at the center of a 2×2 tunnel, the tunnel can be significantly destabilized due to the facilitated Mn^{4+} to Mn^{3+} reduction. Our results highlight the importance of introducing metal ions that are more stable than Mn^{4+}, as they can not only promote the stoichiometry of pristine cryptomelane during synthesis, but also enhance the capacity of the tunnel structure under lithiation conditions. Such

fundamental insight can open new ways to rationally design manganese oxide materials for battery applications.

Conclusions

To conclude, we characterized the structural features of V substituted cryptomelane at atomic levels, identified the shrinkage in nanorod length, reduction of body defects (2×3 and 2×1 tunnels), and increased structural crystallinity upon vanadium substitution. High resolution EELS mapping confirmed the substitution of V for Mn in the tunnel wall, and EDX mapping showed no apparent chemical segregation of V over the scale of the nanorods. Both in-situ and ex-situ lithiation results reveal that Mn is the critical redox species for energy storage capacity. This is consistent with DFT simulations, showing that under lithiation conditions Mn^{4+} acts as an electron acceptor while the V^{4+} substituent is the structural stabilizer that enables the capacity enhancement of the (2×2) tunnel. The higher voltage and improved reversibility of the capacity in V substituted samples confirmed the structural and theoretical rationalization presented herein. Our current results demonstrate the importance of detailed characterization of the material structure to unambiguously establish the correlation between structural motifs and the electrochemical behavior, which is challenging, but essential for rational design of battery materials.

Methods:

Material growth:

Pristine and V-substituted cryptomelane ($K_xMn_8O_{16}$ and $K_xMn_{1-y}V_yO_{16}$) materials were synthesized using a modified version of a previously published reflux method for silver containing α-MnO_2 rods.[36,37] Reagents used in the synthesis were potassium permanganate ($KMnO_4$), 50% (v/v) nitric acid (HNO_3), manganese sulfate monohydrate ($MnSO_4 \cdot H_2O$), and deionized (DI) water. Sodium metavanadate ($NaVO_3$) was used as the vanadium source for the V-substituted reactions. All samples were annealed at 300°C for 6 hours prior to use.

Electrochemical measurements:

A mixture of 80% cryptomelane ($K_xMn_8O_{16}$ or $K_xMn_{1-y}V_yO_{16}$), 10% carbon, and 10% polyvinylidene fluoride (PVDF) was cast onto aluminum foil and used as a cathode. 1M $LiPF_6$ in ethylene carbonate/dimethyl carbonate (3:7 by volume) was used as the electrolyte. Coin cells were assembled in an argon filled glovebox using the cathode, polypropylene separator, and Li metal foil.

Galvanostatic cycling was performed where the depth of discharge was controlled to reach an average oxidation state of $Mn^{3.25+}$ for each material. The expected average oxidation state of Mn was calculated assuming all V^{5+}. The materials were cycled at 20 mA/g to an average oxidation state of $Mn^{3.25+}$ upon discharge and 3.8V upon charge.

DFT simulations:

Spin polarized density functional theory (DFT)[38,39] simulations were preformed using the Vienna Ab-Initio Simulation Package (VASP) code.[40,41] Core electrons defined by Projector augmented wave (PAW)[42] with the generalized gradient approximation (GGA) using Perdew-Burke-Ernzerhof (PBE) functionals.[43] The Kohn-Sham one-electron wave functions were expanded by using a plane wave basis set with a 400 eV kinetic energy cutoff. A 2 × 2 × 6 k-point grid, in the Monkhorst-Pack scheme, was used to sample the Brillouin zone.[44] Atomic positions were optimized until Hellman-Feynman force on every atom was less than 0.01 eV/Å. The following soft potentials used: Mn_sv_GW, V_pv, O_GW, K_sv_GW and Li_sv_GW. A Hubbard correction of U = 5.1 eV and J = 1.2 eV were used for Mn whereas U = 3.25 eV and J = 0 eV were used for V.[45-47]

2 x 2 tunneled cryptomelane was described using a KM_8O_{16} supercell. The V substituted material, KMn_7VO_{16}, was described by exchanging one Mn per supercell with one V. Sequential lithiation starting with the pristine structures yielded lithiated structures with the most stable Li insertion locations after several Li sites were evaluated for each stage. The average voltage was calculated as $[E(Li_nMn_7MO_{16}) – E(Mn_7MO_{16}) - nE(Li)]/nF$, where n is the number of Li in the supercell and F is Faraday's constant.[48,49]

Valence states for Mn and V were determined using the Bader charge analysis.[50] Reference Bader charges for Mn oxide (Mn_3O_4, Mn_2O_3, and MnO_2) and V oxide (V_2O_3, VO_2, and V_2O_5) bulk standards were used for calibration. The oxidation state of Mn and V for each structure was calculated using their calibrated Bader charges. Thermodynamic stability of stoichiometric tunnel structures was evaluated. The formation energies (eV/supercell) for (1) KMn_8O_{16}, (2) KMn_7VO_{16}, and (8) KMn_8VO_{16} were calculated using the following reactions:

(1) $8\ Mn^{2+} + K^+ + 16\ H_2O \rightarrow KMn_8O_{16} + 16\ H_2$

(2) $7\ Mn^{2+} + K^+ + V^{5+} + 16\ H_2O \rightarrow KMn_7VO_{16} + 16\ H_2$

(3) $8\ Mn^{2+} + K^{+} + V^{5+} + 16\ H_2O \rightarrow KMn_8VO_{16} + 16\ H_2$

where the counterions for each ion were not included. The total energies for H_2O, H_2, and hollandite systems were determined from DFT calculations. For each precursor, the total energies for an atom in gas phase were calculated, which were sequentially calibrated by the standard energies of corresponding solvated ions,[51] Mn^{2+} (aq) or $MnSO_4$ (aq), VO_3^- (aq), and K^+ (aq), according to the synthesis procedure for these materials reported previously.[30,31]

Electron microscopy:

The electron microscopy results were mainly collected on a JEOL ARM 200F microscope, operated at 200 kV. Typical scanning transmission electron microscopy (STEM) parameters were: probe size 4C or 8C; condenser lens aperture of 30μm; camera length 6 cm. Some of the STEM images are filtered using a Gaussian function to reduce the high frequency noise. The EELS results were recorded in STEM mode, with entrance aperture size of 5mm, energy dispersion 0.1 eV/channel, core-loss range setting at 500 eV, and with voltage at 200 kV. The high-resolution EELS mapping was processed using principal component analysis method (four components) to improve the image contrast. The in-situ TEM measurements were carried out using a Nanofactory single tilt biasing holder. The powder samples were first dispersed onto a half copper grid. The copper grid with sample was then loaded onto a 3mm-diameter gold wire which was further mounted onto the Nanofactory holder. A tungsten tip was scratched against a lithium foil to provide lithium source and mounted to the holder while inside a glovebox. Before loading the holder into the TEM microscope, the lithium was exposed to air for a few seconds to produce LiO_x electrolyte for the in-situ experiments. A negative bias of -2 V was applied to the device after making contact to facilitate the in-situ experiment.

Acknowledgement

Materials synthesis, electrochemistry, and theory, and the TEM data collected by S.Z.Y. were supported by the Center for Mesoscale Transport Properties, an Energy Frontier Research Center supported by the DOE-BES, under award #DE-SC0012673. The electron microscopes used for structural characterizations are supported by the U.S. Department of Energy, Basic Energy Sciences (DOE-BES), Materials Science and Engineering Division, under Contract #DE-SC0012704. Theory and computational research were done in part at the Center for Functional Nanomaterials, which is a

U.S. DOE Office of Science Facility, and the Scientific Data and Computing Center, a component of the Computational Science Initiative, at Brookhaven National Laboratory under Contract #DE-SC0012704. Part of the calculations were performed using the high-performance LI-red and Handy computing systems at the Institute of Advanced Computational Sciences (IACS) and the SeaWulf cluster at Stony Brook University. Shize Yang would like to thank Xuewen Fu and Shaobo Cheng for providing the VO_2 references. D.M.L. acknowledges the support of the National Science Foundation Graduate Research Fellowship under grant no. 1839287. Any opinions, findings, and conclusions or recommendations expressed in this material are those of the authors and do not necessarily reflect the views of the National Science Foundation.

References

[1] M. S. Whittingham, Chemical Reviews. 104 (2004) 4271.
[2] J. W. Choi, D. Aurbach, Nature Reviews Materials. 1 (2016) 16013.
[3] L. M. Housel, L. Wang, A. Abraham, J. Huang, G. D. Renderos, C. D. Quilty, A. B. Brady, A. C. Marschilok, K. J. Takeuchi, E. S. Takeuchi, Accounts Chem. Res. 51 (2018) 575.
[4] X. Hu, D. A. Kitchaev, L. Wu, B. Zhang, Q. Meng, A. S. Poyraz, A. C. Marschilok, E. S. Takeuchi, K. J. Takeuchi, G. Ceder, Y. Zhu, Journal of the American Chemical Society. 140 (2018) 6961.
[5] S. L. Brock, N. Duan, Z. R. Tian, O. Giraldo, H. Zhou, S. L. Suib, Chemistry of Materials. 10 (1998) 2619.
[6] J. Huang, X. Hu, A. B. Brady, L. Wu, Y. Zhu, E. S. Takeuchi, A. C. Marschilok, K. J. Takeuchi, Chemistry of Materials. 30 (2018) 366.
[7] C. S. Johnson, Journal of Power Sources. 165 (2007) 559.
[8] J. E. Post, Proceedings of the National Academy of Sciences. 96 (1999) 3447.
[9] M. M. Thackeray, Progress in Solid State Chemistry. 25 (1997) 1.
[10] M. M. Thackeray, J. R. Croy, E. Lee, A. Gutierrez, M. He, J. S. Park, B. T. Yonemoto, B. R. Long, J. D. Blauwkamp, C. S. Johnson, Y. Shin, W. I. F. David, Sustainable Energy & Fuels. 2 (2018) 1375.
[11] L. Athouël, F. Moser, R. Dugas, O. Crosnier, D. Bélanger, T. Brousse, The Journal of Physical Chemistry C. 112 (2008) 7270.
[12] Q. Feng, H. Kanoh, K. Ooi, J. Mater. Chem. 9 (1999) 319.
[13] X. Hu, J. Huang, L. Wu, M. Kaltak, M. V. Fernandez-Serra, Q. Meng, L. Wang, A. C. Marschilok, E. S. Takeuchi, K. J. Takeuchi, M. S. Hybertsen, Y. Zhu, Chemistry of Materials. 30 (2018) 6124.
[14] S. L. Suib, Annu. Rev. Mater. Sci. 26 (1996) 135.
[15] S. L. Suib, Accounts Chem. Res. 41 (2008) 479.
[16] J. A. Dawson, P. Canepa, T. Famprikis, C. Masquelier, M. S. Islam, Journal of the American Chemical Society. 140 (2018) 362.
[17] M. Okubo, E. Hosono, J. Kim, M. Enomoto, N. Kojima, T. Kudo, H. Zhou, I. Honma, Journal of the American Chemical Society. 129 (2007) 7444.
[18] K. T. Lee, J. Cho, Nano Today. 6 (2011) 28.
[19] K. Xu, Chemical Reviews. 114 (2014) 11503.
[20] J.-Y. Piao, Y.-G. Sun, S.-Y. Duan, A.-M. Cao, X.-L. Wang, R.-J. Xiao, X.-Q. Yu, Y. Gong, L. Gu, Y. Li, Z.-J. Liu, Z.-Q. Peng, R.-M. Qiao, W.-L. Yang, X.-Q. Yang, J. B. Goodenough, L.-J. Wan, Chem. 4 (2018) 1685.
[21] Y. Lyu, Y. Liu, L. Gu, Chinese Physics B. 25 (2016) 018209.

[22] P. Yan, J. Zheng, J. Liu, B. Wang, X. Cheng, Y. Zhang, X. Sun, C. Wang, J.-G. Zhang, Nature Energy. 3 (2018) 600.
[23] S.-Z. Yang, Y. Gong, P. Manchanda, Y.-Y. Zhang, G. Ye, S. Chen, L. Song, S. T. Pantelides, P. M. Ajayan, M. F. Chisholm, W. Zhou, Advanced Materials. 30 (2018) 1803477.
[24] S.-Z. Yang, W. Sun, Y.-Y. Zhang, Y. Gong, M. P. Oxley, A. R. Lupini, P. M. Ajayan, M. F. Chisholm, S. T. Pantelides, W. Zhou, Physical Review Letters. 122 (2019) 106101.
[25] C. Yi, Z. Shiyong, J. Bernt, V. Jean-Pierre, S. Martin, R. M. R., C. Min, L. Chang, C. M. F., M. Roland, C. Hui-Ming, Y. Shi-Ze, J. S. Ping, Advanced Materials. 30 (2018) 1706287.
[26] Y. Yuan, C. Liu, B. W. Byles, W. Yao, B. Song, M. Cheng, Z. Huang, K. Amine, E. Pomerantseva, R. Shahbazian-Yassar, J. Lu, Joule. 3 (2019) 471.
[27] A. Gloter, V. Serin, C. Turquat, C. Cesari, C. Leroux, G. Nihoul, The European Physical Journal B - Condensed Matter and Complex Systems. 22 (2001) 179.
[28] M. Polverejan, J. C. Villegas, S. L. Suib, Journal of the American Chemical Society. 126 (2004) 7774.
[29] Z. Hu, X. Xiao, L. Huang, C. Chen, T. Li, T. Su, X. Cheng, L. Miao, Y. Zhang, J. Zhou, Nanoscale. 7 (2015) 16094.
[30] A. S. Poyraz, J. Huang, S. Cheng, L. Wu, X. Tong, Y. Zhu, A. C. Marschilok, K. J. Takeuchi, E. S. Takeuchi, Journal of The Electrochemical Society. 164 (2017) A1983.
[31] A. S. Poyraz, J. Huang, C. J. Pelliccione, X. Tong, S. Cheng, L. Wu, Y. Zhu, A. C. Marschilok, K. J. Takeuchi, E. S. Takeuchi, Journal of Materials Chemistry A. 5 (2017) 16914.
[32] A. B. Brady, K. R. Tallman, E. S. Takeuchi, A. C. Marschilok, K. J. Takeuchi, P. Liu, The Journal of Physical Chemistry C. (2019).
[33] S.-Y. Lee, L. Wu, A. S. Poyraz, J. Huang, A. C. Marschilok, K. J. Takeuchi, E. S. Takeuchi, M. Kim, Y. Zhu, Advanced Materials. 29 (2017) 1703186.
[34] L. Wu, F. Xu, Y. Zhu, A. B. Brady, J. Huang, J. L. Durham, E. Dooryhee, A. C. Marschilok, E. S. Takeuchi, K. J. Takeuchi, ACS Nano. 9 (2015) 8430.
[35] L. Laffont, P. Gibot, Materials Characterization. 61 (2010) 1268.
[36] K. J. Takeuchi, S. Z. Yau, M. C. Menard, A. C. Marschilok, E. S. Takeuchi, ACS Appl Mater Interfaces. 4 (2012) 5547.
[37] H. C. Genuino, Y. Meng, D. T. Horvath, C.-H. Kuo, M. S. Seraji, A. M. Morey, R. L. Joesten, S. L. Suib, ChemCatChem. 5 (2013) 2306.
[38] P. Hohenberg, W. Kohn, Physical Review. 136 (1964) B864.
[39] W. Kohn, L. J. Sham, Physical Review. 140 (1965) A1133.
[40] G. Kresse, J. Furthmüller, Computational Materials Science. 6 (1996) 15.
[41] G. Kresse, J. Furthmüller, Physical Review B. 54 (1996) 11169.
[42] P. E. Blöchl, Physical Review B. 50 (1994) 17953.
[43] J. P. Perdew, K. Burke, M. Ernzerhof, Physical Review Letters. 77 (1996) 3865.
[44] H. J. Monkhorst, J. D. Pack, Physical Review B. 13 (1976) 5188.
[45] A. Jain, S. P. Ong, G. Hautier, W. Chen, W. D. Richards, S. Dacek, S. Cholia, D. Gunter, D. Skinner, G. Ceder, K. A. Persson, APL Materials. 1 (2013) 011002/1.
[46] A. B. Brady, K. R. Tallman, E. S. Takeuchi, A. C. Marschilok, K. J. Takeuchi, P. Liu, The Journal of Physical Chemistry C. (2019).
[47] M. Kaltak, M. Fernández-Serra, M. S. Hybertsen, Physical Review Materials. 1 (2017) 075401/1.
[48] H. Guo, Y. Zhang, A. C. Marschilok, K. J. Takeuchi, E. S. Takeuchi, P. Liu, Phys Chem Chem Phys. 19 (2017) 26322.
[49] Y. Zhang, C. J. Pelliccione, A. B. Brady, H. Guo, P. F. Smith, P. Liu, A. C. Marschilok, K. J. Takeuchi, E. S. Takeuchi, Chem. Mater. 29 (2017) 4282.
[50] M. Yu, D. R. Trinkle, The Journal of Chemical Physics. 134 (2011) 064111/1.
[51] J. A. Dean, *Lange's handbook of chemistry*, McGraw-Hill, New York **1985**.

Figures

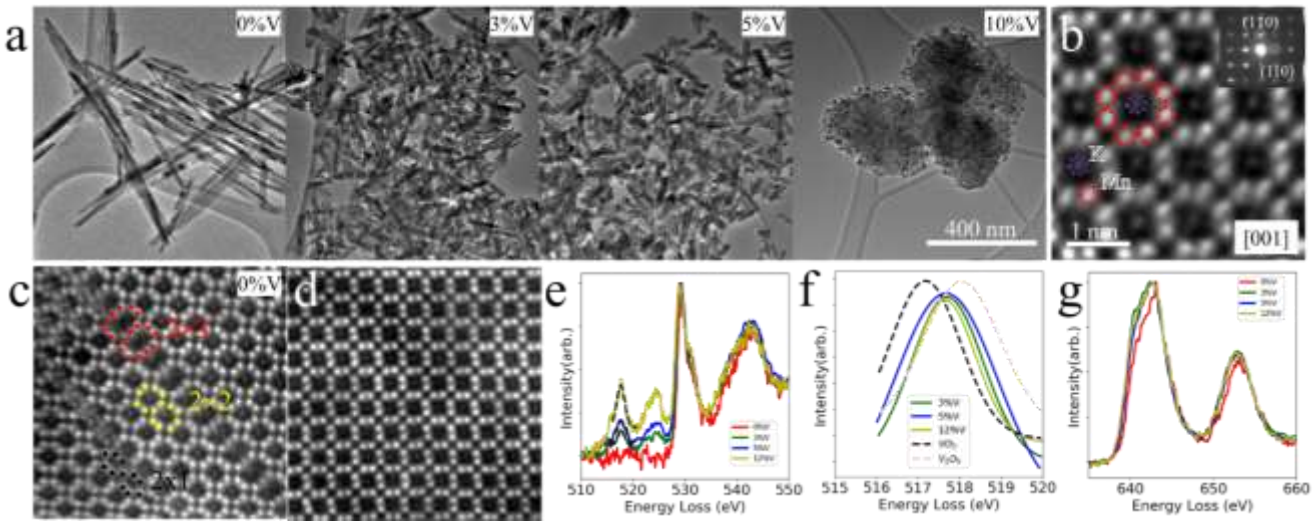

Figure 1. (a) Typical TEM images of four samples at field of view of 920 nm: 0%V-substituted ($K_{0.99}Mn_8O_{16}$); 3%V- substituted ($K_{1.00}Mn_{7.78}V_{0.22}O_{16}$); 5%V- substituted ($K_{1.02}Mn_{7.63}V_{0.37}O_{16}$); 10%V- substituted ($K_{0.97}Mn_{7.2}V_{0.8}O_{16}$); (b) Typical STEM-ADF image of the 2×2 tunnels and typical nanobeam electron diffraction (upper-inset); (c) Typical STEM-ADF image of 0%V samples with irregular 2×1 and 2×3 tunnels; (d) Typical STEM-ADF image of samples with V dopants where no irregular tunnels are identified; (e) The electron energy loss spectroscopy of O-K edge and V-L edge; (f) The V-L_3 peak is fitted with a Gaussian function and plotted together with VO_2 and V_2O_5 reference samples, V is determined to be at $V^{4.6+}$ for all substituted samples; (g) The slight increase of peak intensity around 640 eV indicates the reduction of Mn valence upon vanadium substitution.

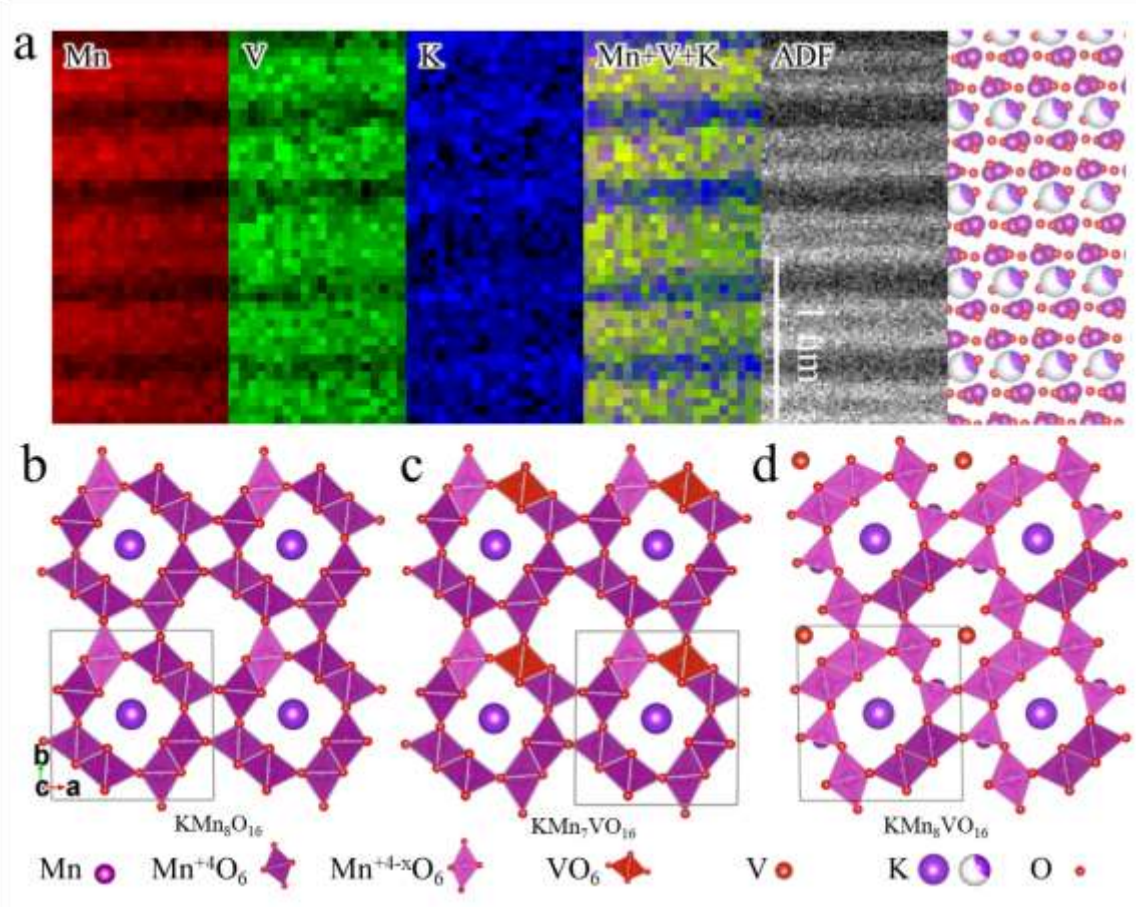

Figure 2. (a) STEM EELS mapping results for the 5%V- substituted sample ($K_{1.02}Mn_{7.63}V_{0.37}O_{16}$) showing Mn (red), V (green) and K (blue) with composite (Mn-V-K), and related ADF image and structural models shown to the right; (b) Structural model for pristine cryptomelane (KMn_8O_{16}), with K^+ in the tunnel highlighted as a large ball and the reduced Mn shown in semi-transparent polyhedra; (c) Structural model for V-substituted cryptomelane (KMn_7VO_{16}), with dopant in the tunnel wall shown as red polyhedra; (d) Structural model for V-centered cryptomelane (KMn_8VO_{16}), with dopant in the tunnel shown as red ball.

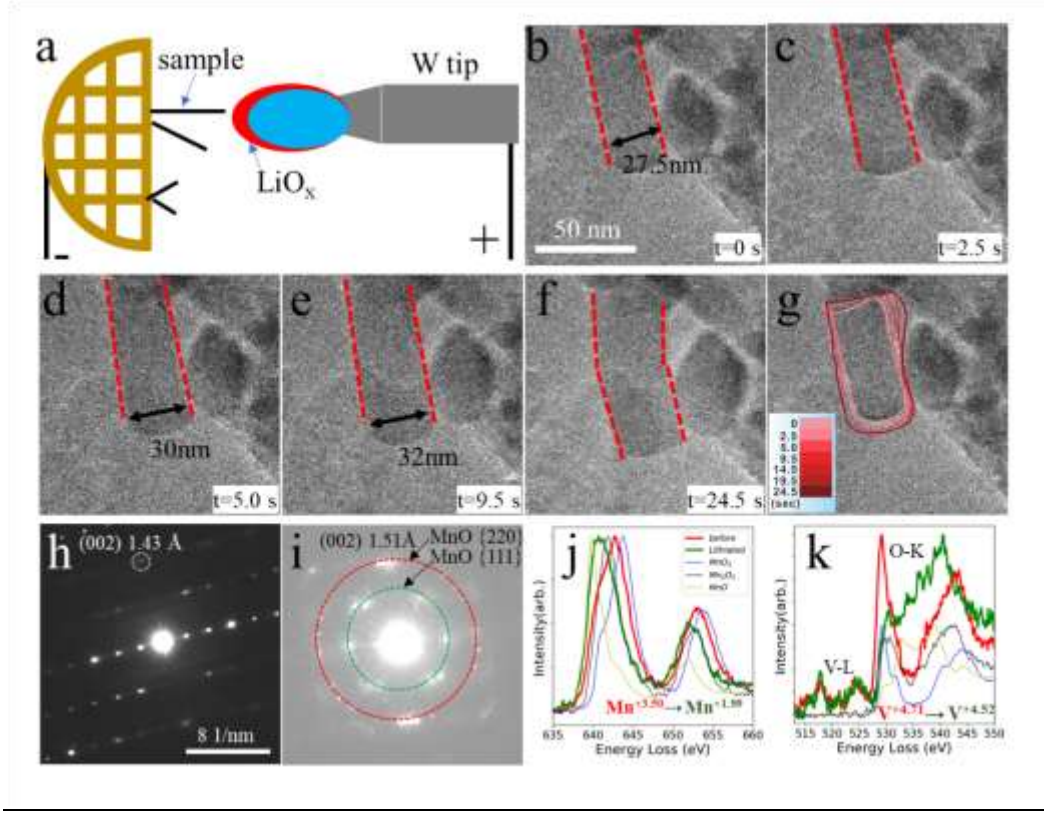

Figure 3. (a) Schematic for the in-situ TEM experimental setup; (b-f) In-situ recorded images showing the gradual lithiation process of 5%V- substituted cryptomelane ($K_{1.02}Mn_{7.63}V_{0.37}O_{16}$); (g) Morphology change of the nanorod upon lithiation with highlighted outlines; Nano beam electron diffraction (NBED) was recorded on the single nanorod before (h) and after (i) lithiation; (j-k) The EELS spectra for V-L edge, O-K edge, and Mn-L edge before and after lithiation with standard reference MnO_2, Mn_2O_3, and MnO samples. The energy shift towards lower energy for Mn-L edge after lithiation indicates the reduction of Mn.

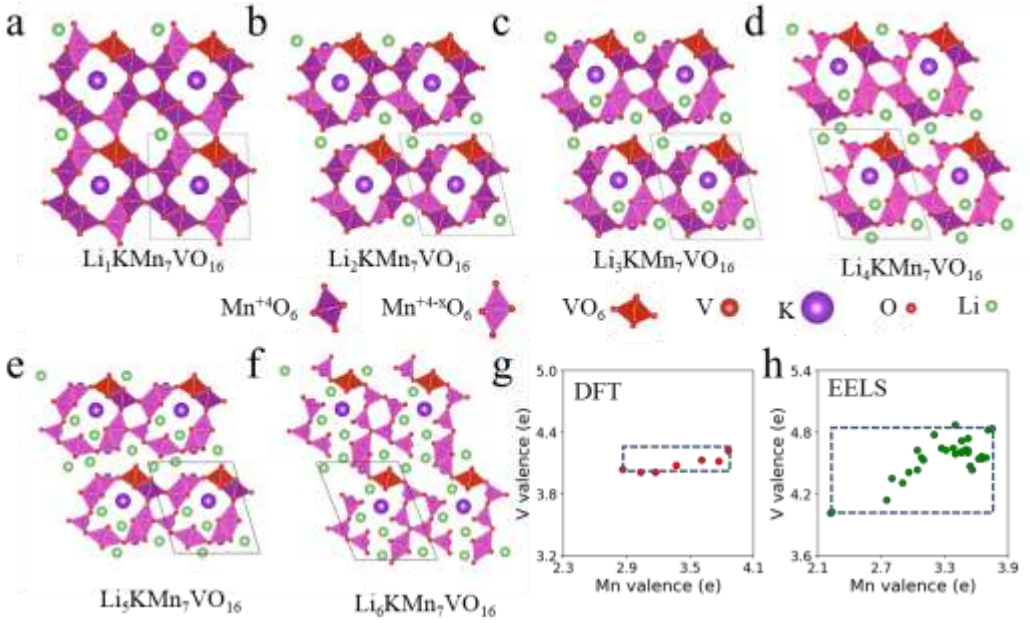

Figure 4. (a-f) Relaxed structure models by DFT simulation with different numbers of inserted Li atoms; (g) The correlation between Mn and V valence from DFT results; (h) The correlation between Mn and V valence measured from lithiated samples by EELS. The valence span is set to 1.8 e for both horizontal and vertical axis in (g) and (h) for clear visual comparison.